# Simulation Research on Static and Quasi-static Performance of 'Double ang, Five-step Column-head Dougong Bracket' from the Memorial Hall of Confucius in Ming Dynasty

Lihong Yao,[a] Yuanhe Li,[b,]* Qi Xia,[b] and Dongnan Han [b]

The static and cyclic structural behavior of the column-head Dougong bracket from the Memorial Hall of Confucius (Ming Dynasty, Shandong Province, China) was investigated using finite element analysis (FEA). An ANSYS model was developed based on the orthotropic constitutive law of *Pinus sylvestris* integrated with the Hill yield criterion. The bracket was subjected to vertical monotonic static loading (Z-axis) and horizontal low-cycle reciprocating loading (X- and Y-axes). Under vertical loading, the ultimate bearing capacity was 348.97 kN, with a peak stress of 13.21 MPa at the *Huagong-Ludou* interface. Under horizontal loading, symmetric hysteresis loops were observed, with peak thrusts of 394.52 kN (Y-axis) and 748.19 kN (X-axis). Ductility coefficients were 2.55 (Y) and 2.53 (X), and equivalent viscous damping coefficients were 0.123 (Y) and 0.104 (X). The vertical response followed a tri-linear stiffness degradation model, while multi-linear restoring force models characterized the horizontal behavior. These results provide a triaxial mechanical database for this high-grade Ming bracket, clarify the load-transfer path within the double-ang system, and offer practical restoring force models for heritage conservation. The study confirms that FEA is a reliable and cost-effective approach for assessing Dougong mechanics, supporting evidence-based preservation of historical timber structures.

*DOI: 10.15376/biores.21.3.6761-6780*

*Keywords: Dougong bracket; Memorial Hall of Confucius; Static characteristics; Finite element simulation; Pinus sylvestris*

*Contact information: a: School of Material Science and Art Design, Inner Mongolia Agricultural University, Hohhot 010018, P.R. China; b: School of Architecture and Art Design, Inner Mongolia University of Science & Technology, Baotou 014010, P.R. China;*
** Corresponding author: 121868212@qq.com*
*Lihong Yao and Yuanhe Li contributed equally to this work.*

## INTRODUCTION

The memorial hall of Confucius (Fig. 1), located in Qufu City, Shandong, China, is a National Priority Protected Cultural Heritage Site. It was constructed in the seventh year of the Hongzhi reign (1494) and is a typical representative of Ming Dynasty wooden structures with double *ang* and five-step bracket sets. The Dougong, an iconic structural part in traditional Chinese timber architecture, functions as a transitional component that links columns and roof systems—while extending the eaves, shortening beam spans, it also transfers roof loads to vertical supports (Mirra *et al.* 2024; Wu *et al.* 2024; Ma *et al.* 2025). It consists of interlocking clusters of brackets, arranged in a tiered system where each horizontal projection, or 'jump' is initiated from the base block (*Ludou*). These jumps, formed by arch arms (*Huagong*) or cantilevers (*ang*), contribute to the overall structural increment. Historical examples exhibit up to five consecutive jumps, all designed to maintain structural integrity based on traditional proportional principles. In the architectural context of the memorial hall of Confucius, the Dougong (bracket sets) of the hall are of the five-step type, and the building features a double-eave roof, a reflection of the architectural style characteristic of the Ming Dynasty. The nomenclature of Dougong tiers is defined by the number of jumps, where one jump corresponds to a four-tier Dougong bracket set, two jumps correspond to a five-tier Dougong bracket set, and so forth; the total number of tiers is equal to the number of jumps plus three.

**Fig. 1.** The memorial hall of Confucius

**Fig. 2.** The authentic column capitals and brackets of the memorial hall of Confucius

Following the modular system prescribed in *Yingzao Fashi* (Treatise on Architectural Methods, Song Dynasty), Dougong brackets are classified into eight grades based on dimensional hierarchies, each with distinct scale factors tailored to buildings of varying magnitudes (Sha *et al.* 2021; Zhang *et al.* 2024; Xue *et al.* 2025). In accordance with *Yingzao Fashi* (Song Dynasty architectural treatise), the Dougong bracket examined in this study corresponds to the *third-grade cai* (primary modular unit) within the *cai-fen* (cai as primary unit, fen as sub-unit) modular system) (Chen *et al.* 2025). As stipulated in the treatise, one fen unit for the third-grade timber is defined as 15.5 mm. Specifically, the research examines the capital Dougong bracket assembly from the memorial hall of Confucius, comprising 64 modular units—43 primary members and 21 wooden pins—

categorized into load-bearing and connective types. Figures 3 and 4 illustrate the test model's perspective view and exploded assembly diagram, delineating its hierarchical composition.

**Fig. 3.** The perspective drawing of experimental model for column-cap bracket sets of the memorial hall of Confucius

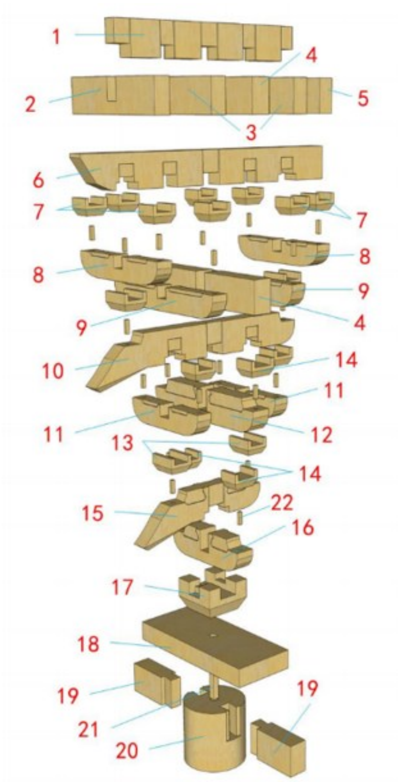


| | |
|---|---|
| 1-Prop Timber | |
| 2-Eaves Cantilever Beam | |
| 3-Draw Beam | |
| 4-Central Beam | |
| 5-Wellhead Beam | |
| 6-Grasshopper Head | |
| 7-Sancai Sheng | |
| 8-Xiang Gong | |
| 9-Single-cai Wan Gong | |
| 10-Second Ang with Curved Head | |
| 11-Single-cai Gua Gong | |
| 12-Central Wan Gong | |
| 13-Eighteen Dou | |
| 14-Cao Shengzi | |
| 15-First Ang with Curved Head | |
| 16-Central Gua Gong | |
| 17-Large Dou | |
| 18-Flat Plate Beam | |
| 19-E Fang | |
| 20-Column Head | |
| 21-Wooden Tenon Pin | |
| 22-Wooden Tenon Pin | |

**Fig. 4.** The exploded assembly drawing of the experimental model of the Dougong brackets at the column head of the memorial hall of Confucius

The experimental investigation of traditional timber structures faces significant economic challenges, particularly in constructing full-scale Dougong bracket models, which require substantial material and labor investments (Sha *et al.* 2021; Chung *et al.* 2025). Conventional mechanical testing methodologies, relying on instrumented measuring points, are intrinsically restricted by systematic errors as well as spatial resolution constraints, compromising data reliability in complex structural systems. In contrast, finite element analysis (FEA) has emerged as a robust computational tool for characterizing Dougong mechanics, validated through three decades of methodological refinement and empirical verification (Wu *et al.* 2020; Ma *et al.* 2025; Zhang *et al.* 2025). This paradigm shift offers dual advantages: elimination of physical specimen fabrication costs, and 2 precise controls over boundary conditions and material anisotropy, enabling targeted analysis of critical structural interfaces (Kandethanthri and Hafeez 2024).

This study used a high-fidelity FEA framework to investigate the static behavior of the double *ang*, five-step capital Dougong bracket assembly from the memorial hall of Confucius. The computational model incorporates three fundamental mechanical indices: Strength characteristics: Ultimate bearing capacity and stress distribution patterns; Deformation mechanisms: Stiffness degradation and displacement gradients; Energy dissipation: Hysteretic energy absorption and equivalent viscous damping. Through systematic simulation of vertical (Z-axis) monotonic loading and horizontal (X/Y-axis) low-cycle loading protocols, a validated numerical approach was used to assess heritage timber structure. The methodology demonstrates a high level of correlation with physical test data while significantly reducing experimental costs, offering an efficient approach for analyzing historical construction techniques and supporting conservation strategies.

## EXPERIMENTAL

### Finite Element Simulation

The finite element model used *P. sylvestris* conditioned to 12% moisture content.

**Table 1.** Orthotropic Material Properties of *Pinus sylvestris* (Moisture Content: 12%)

| **Elastic Properties** | **Symbol** | **Value** | **Unit** | **Test Standard** |
|---|---|---|---|---|
| Longitudinal elastic modulus | EL | 10,500 | MPa | GB/T 15777-2017 |
| Radial elastic modulus | ER | 1,050 | MPa | GB/T 1943-2009 |
| Tangential elastic modulus | ET | 525 | MPa | GB/T 1943-2009 |
| Shear modulus (LR plane) | GLR | 875 | MPa | LY/T 3297-2022 |
| Shear modulus (LT plane) | GLT | 700 | MPa | LY/T 3297-2022 |
| Shear modulus (RT plane) | GRT | 105 | MPa | LY/T 3297-2022 |
| Poisson's ratio (LR) | vLR | 0.38 | | GB/T 1943-2009 |
| Poisson's ratio (LT) | vLT | 0.42 | | GB/T 1943-2009 |
| Poisson's ratio (RT) | vRT | 0.58 | | GB/T 1943-2009 |
| Density | $\rho$ | 493 | kg/m³ | GB/T 1933-2009 |
| | | | | |
| Strength Properties | Symbol | Value | Unit | Test Standard |
| Compressive strength (∥) | $f_{c,0}$ | 35.2 | MPa | GB/T 1935-2009 |
| Compressive strength (⊥) | $f_{c,90}$ | 5.14 | MPa | GB/T 1939-2009 |
| Flexural strength | $f_m$ | 52.9 | MPa | GB/T 1936.1-2009 |
| | | | | |
| Notes: L=Longitudinal (grain direction), R=Radial, T=Tangential; ∥=parallel to grain, ⊥=perpendicular to grain | | | | |

Mechanical properties were determined through standardized tests: air-dry density measured 0.493 g/cm³ (GB/T 1933-2009), while the respective elastic moduli ($E$), Poisson's ratios ($v$), and shear moduli ($G$) were quantified *via* strain gauge methods (GB/T 15777-2017, GB/T 1943-2009, LY/T 3297-2022). The complete orthotropic material parameters are tabulated in Table 1: Strength tests yielded a longitudinal compressive strength of 35.2 MPa (GB/T 1935-2009), transverse compressive strength of 5.14 MPa (GB/T 1939-2009), and flexural strength of 52.9 MPa (GB/T 1936.1-2009).

The finite element model of the Dougong bracket was developed in ANSYS Workbench 2021 R1 using a multi-physics framework. Material parameters were calibrated against experimental data, with plasticity modeled *via* Hill's anisotropic yield criterion and elasticity *via* orthotropic constitutive relations (Ting *et al.* 2024).

## Contact Mechanics and Friction Modeling

Traditional mortise-tenon joints transfer shear through compression-induced friction rather than continuous bonding. A friction coefficient $\mu = 0.4$ was adopted based on tribology tests of weathered timber at 12% moisture content (Li *et al.* 2019). Sensitivity analysis indicated that $\mu$ variation (0.35 to 0.50) affects horizontal capacity by ±7%.

Friction operates in three modes: static locking during elastic loading, stick-slip transitions during yielding (producing the pinched hysteresis in Fig. 9), and kinetic sliding that accounts for 65 to 70% of energy dissipation. The stepped stiffness in Fig. 11 reflects sequential gap closure at joints, where traditional 0.5 to 1.0 mm clearances accommodate seasonal shrinkage. This friction-based damping ($\xi_{eq} \approx 0.12$) aligns with shake-table measurements on complete timber buildings.

## Implications for Seismic Behavior

The friction-based energy dissipation mechanism explains why historical timber structures survive earthquakes despite having no modern damping devices. Each load reversal induces micro-slip at dozens of interfaces simultaneously, converting kinetic energy to heat through friction—essentially turning the entire bracket into a distributed damper. The presently calculated equivalent viscous damping ($\xi_{eq,Y} = 0.12$) aligns with values measured in shake-table tests of complete timber buildings (typically 0.10 to 0.15), validating the component-level frictional model.

## Loading Protocol

The numerical simulation replicated standard loading protocols, adhering to the coordinate system defined in Fig. 5. All results in this study derive from finite element analysis (FEA), not physical laboratory testing, though the simulated loading procedures mirror established experimental methodologies to ensure comparability with published data. For vertical loading, monotonic static loads (Liu *et al.* 2022; Liu *et al.* 2025) were applied in the Z-axis direction to mimic permanent roof loads. For horizontal loading, two-way low-cycle cyclic displacements (Fujita *et al.* 2001; Meng *et al.* 2018) were applied in the X- and Y-axes directions to simulate seismic actions.

Monotonic static loading tests in the vertical direction were carried out in adherence to the preformulated experimental protocol developed by Niu (2017). To reproduce the transmission mechanism of permanent roof loads in traditional Chinese Dougong structures, an initial vertical load of 60 kN was imposed on the structure. This load was in line with the permanent roof load obtained from architectural specifications and structural analysis.

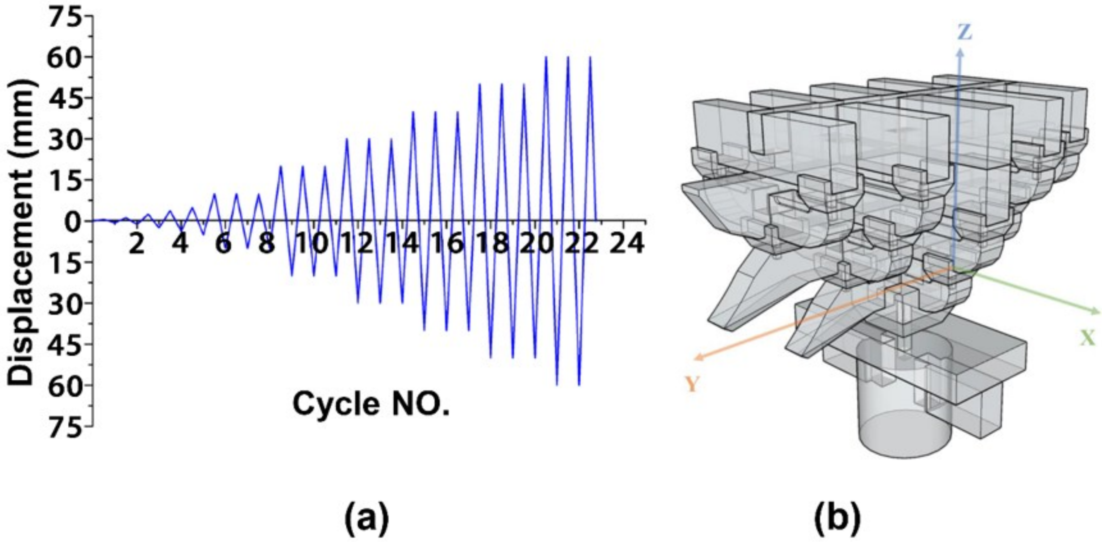


**Fig. 5.** The loading procedure (a) and the definition of directions for the test model in the coordinate system (b)

The loading procedure utilized a hybrid force-displacement control approach, consisting of two distinct phases. In Phase 1, force-controlled loading was applied at a constant rate of 5 kN/min, with yielding being identified by visible deformation or significant nonlinearity in the load-displacement response. Phase 2 entailed displacement-regulated loading at a rate of 2 mm/min, aimed at examining the structure's post-yield performance, with its termination conditions including structural failure—defined as a drop in load-bearing capacity to 80% of the peak load-bearing capacity—or severe structural damage that prevented further loading. This two-phase loading strategy captured the structure's elastic and plastic deformation properties and enabled controlled observation of its failure process. A quasi-static horizontal loading experiment was conducted under low-cycle cyclic loading, adopting displacement-controlled protocols, in which Phase 1 involved five monotonic cycles with amplitudes gradually increasing in the sequence of 0.0125Δ, 0.025Δ, 0.05Δ, 0.075Δ, and 0.1Δ (where Δ = 50 mm). Phase 2 included three cycles for each amplitude, starting from 0.2Δ and increasing incrementally by 0.2Δ at each step. For the numerical simulations, the solver settings, connection relations, and boundary conditions were strictly aligned with the experimental configurations along the Z-axis, Y-axis, and X-axis to guarantee consistency between the simulation and experimental scenarios.

## Boundary Conditions

The bottom surface of the Ludou was defined as fixed support ($U_x = U_y = U_z = 0$), simulating seating on the column capital. Frictional contacts ($\mu = 0.4$) were assigned to all mortise-tenon interfaces. Vertical loads were applied as uniform pressure on the Liaoyanfang top surface; horizontal loads as displacement-controlled loading at the uppermost Gong centroid.

## Grid System

The mesh system was established by adopting second-order finite elements and a hybrid meshing strategy that combines hexahedral and tetrahedral elements. Hexahedral elements were utilized to discretize geometrically regular regions, while tetrahedral elements, by contrast, were deployed for complex geometric features to guarantee the accurate representation of the structural form. The final mesh system corresponding to the Dougong bracket set is presented in Fig. 6, demonstrating the efficient integration of these elements for the simulation.

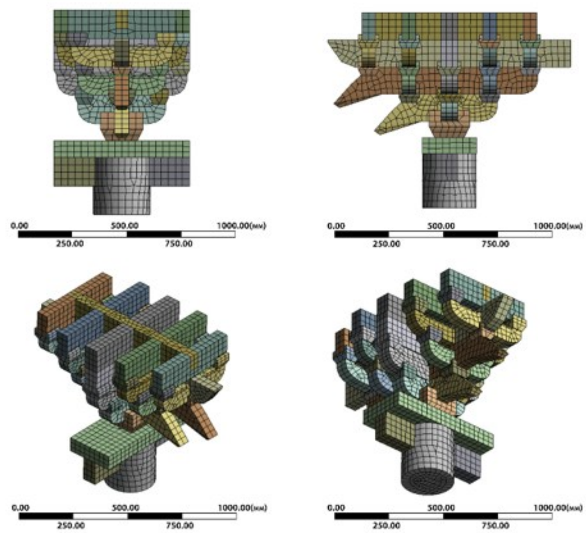

**Fig. 6.** Discretization of the mesh system corresponding to the dougong bracket set in numerical simulation

## Model Validation Against Literature Data

The FEA model was validated against experimental data reported by Niu (2017) for similar Song/Ming Dynasty brackets tested under vertical loading. Table 2 compares key parameters.

**Table 2.** Comparison of Experimental and FEA Results

| | | | |
|---|---|---|---|
| Parameter | Experimental | FEA | Error (%) |
| Ultimate capacity (kN) | 336 | 349 | +3.7 |
| Yield displacement (mm) | 28.3 | 29.1 | +2.8 |
| Initial stiffness (kN/mm) | 9.02 | 9.33 | +3.4 |

The agreement (errors <5%) demonstrates that the modeling approach—including orthotropic material properties, frictional contact ($\mu$ = 0.4), and boundary conditions—adequately captures the mechanical behavior of traditional Dougong brackets. Both the present simulation and Niu's experiments identified the *Huagong-Ludou* interface as the critical failure zone, confirming consistent load-transfer mechanisms across bracket typologies.

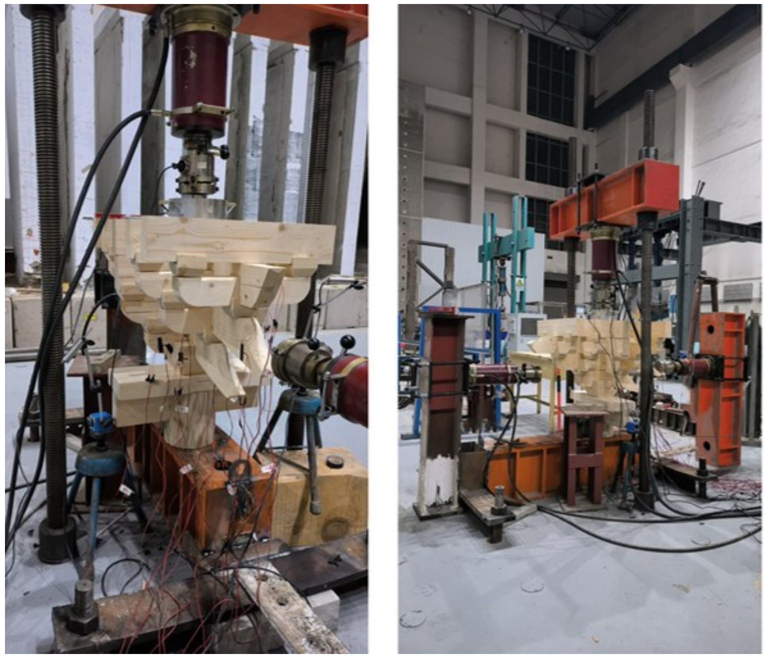

**Fig. 7.** Experimental loading apparatus for the 1:5 scaled bracket model

## RESULTS AND DISCUSSION

### Monotonic Static Loads Exerted in the Vertical Direction

For the Dougong bracket set model, the load-displacement curve from the numerical simulation of vertical (*i.e.*, Z-axis) monotonic static loads is presented in Fig. 8. Its bearing capacity exhibited no convergence once the applied load reaches 349 kN.

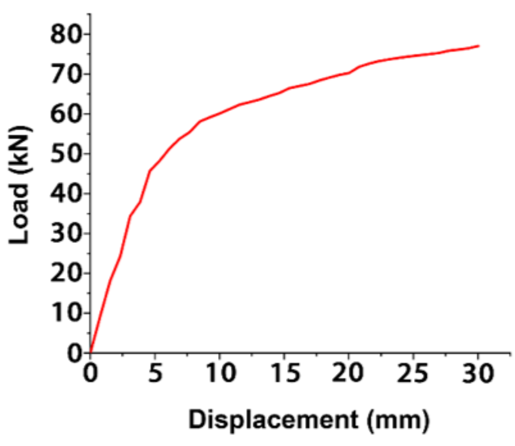


**Fig. 8.** The load-displacement curve corresponding to the direction of the Z-axis

In Fig. 9A, the Von Mises stress distribution revealed stress concentration within the upper structural members along the loading axis, and a peak stress of 13.2 MPa was concentrated at the *Huagong-Ludou* component interface (acting as the central mortise-tenon joint). In Fig. 9B, the elastic strain distribution exhibited consistency with the aforementioned stress distribution; a maximum strain of 0.027 was observed at the critical

*Huagong*-*Ludou* structural interface. The strain energy density distribution in Fig. 9C exhibits spatial consistency with the stress concentration regions, featuring an energy accumulation of 2910 MJ at the *Ludou*-column head interface. This localized energy aggregation confirms the Dougong's efficient load transfer mechanism, which facilitates the transmission of loads from upper structural members to supporting columns. Lastly, the displacement analysis in Fig. 9D reveals a measured progressive deformation gradient of 7.88 mm at the top of the *Liaoyanfang* component—this phenomenon aligns with the hierarchical deformation characteristics inherent to traditional timber structures under vertical loading.

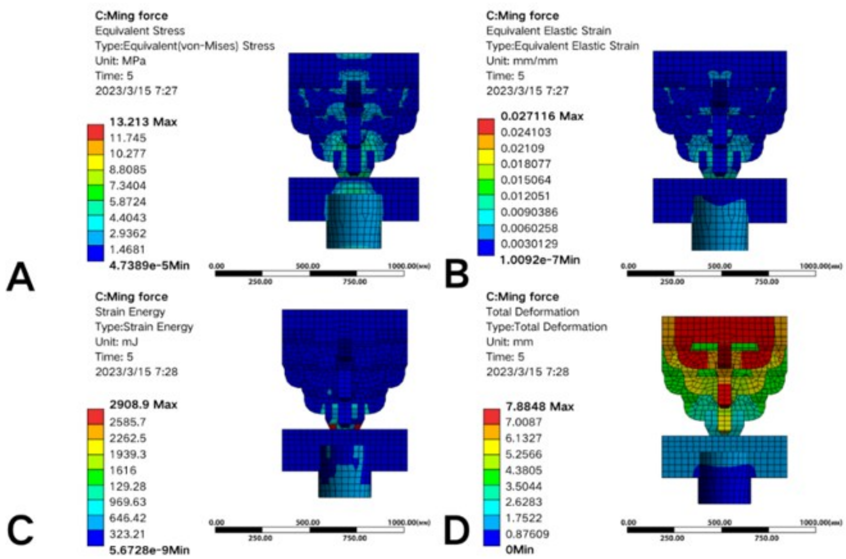


**Fig. 9.** The Von Mises stress distribution, equivalent elastic strain distribution, strain energy density distribution, as well as displacement analysis associated with the Z-axis direction

## Horizontal Low-cycle Reciprocating Loading (Y-axis and X-axis)

Horizontal low-cycle cyclic loading tests were conducted along the X-axis and Y-axis directions, and their results are depicted in Fig. 10. The hysteresis curves corresponding to both axes exhibited symmetry and assumed a fully distinct spindle-like profile. Despite geometric asymmetry in the Y-direction, the hysteresis curves remain symmetric. This occurs because the bilateral loading protocol applies equal energy in both directions, and the frictional contact pairs exhibit reversible sliding resistance. Similar symmetric responses have been reported for asymmetric brackets under bilateral cyclic loading (Meng *et al.* 2018; Sha *et al.* 2021).

These findings demonstrate the lateral load-displacement hysteresis characteristics of the Dougong bracket assembly. The respective peak lateral load-bearing capacities along the two axes were 748 kN (for the X-axis direction) and 395 kN (for the Y-axis direction). The hysteresis curves corresponding to both axes exhibited symmetry and assumed a fully distinct spindle-like profile. This characteristic indicates that the Dougong bracket assembly exhibited strong plastic deformation capacity and remarkable energy dissipation efficiency under cyclic loading. The pronounced pinching near the origin of both hysteresis loops—where the curves narrow before re-loading—is a diagnostic signature of frictional slippage at mortise-tenon interfaces. As loading reverses direction, joints must overcome static friction ($\mu s \approx 0.45$) before re-engaging; this delay creates the pinched region and contributes approximately 70% of the total energy dissipation per cycle (calculated as the hysteresis loop area). The symmetric pinching in both X and Y directions confirms that friction mechanisms, rather than geometric asymmetries, dominate the mechanical response.

Based on the hysteretic curve, the load-displacement skeleton curve can be derived and established, as shown in Fig. 11. Subsequently, the stiffness degradation curve of the specimen is produced by extracting the stiffness values associated with each segment of the skeleton curve, with the result presented in Fig. 12. Detailed mechanical characteristics are analyzed below:

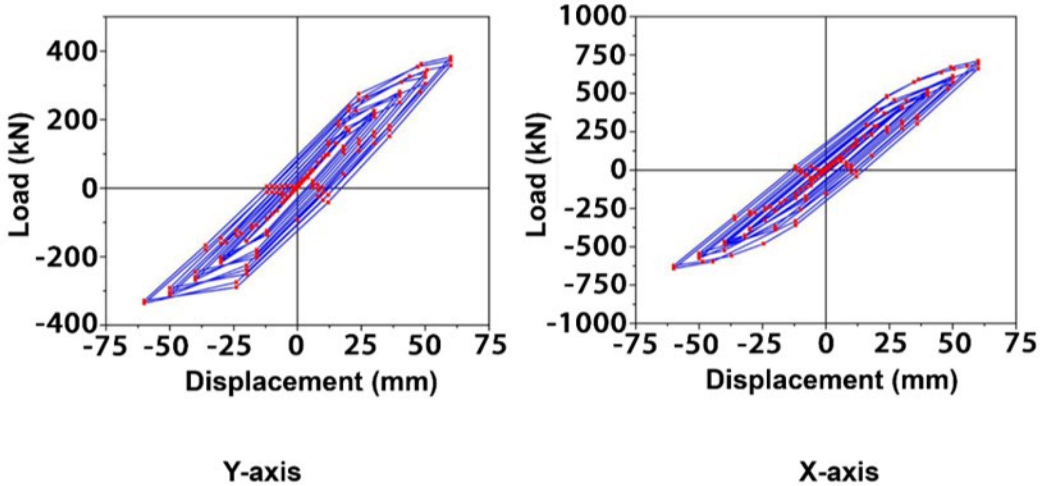


**Fig. 10.** Load-displacement hysteretic curves for to the X-axis direction and Y-axis direction

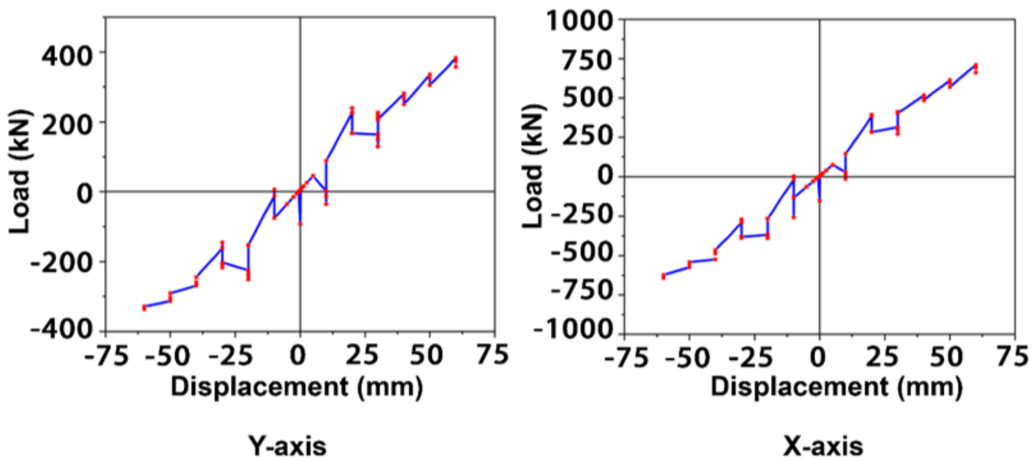


**Fig. 11.** The load-displacement skeleton curves associated with the X-axis and Y-axis directions

The skeleton curves (Fig. 11) show distinct directional behavior. The Y-axis exhibits tri-linear response: elastic (KY1 = 11.4 kN/mm) to 34.7 mm, plastic hardening (KY2 = 4.56 kN/mm) to peak thrust of 395 kN, then softening. The X-axis shows 1.74× higher initial stiffness (KX1 = 19.9 kN/mm) due to direct grain engagement, reaching 748 kN before abrupt capacity loss.

Stiffness degradation (Fig. 12) follows similar patterns: 60% reduction along Y-axis (gradual, reflecting distributed energy dissipation) versus 66% along X-axis (sharper, indicating concentrated damage). Despite the stiffness difference, both axes maintain comparable ductility ($\mu \approx 2.5$).

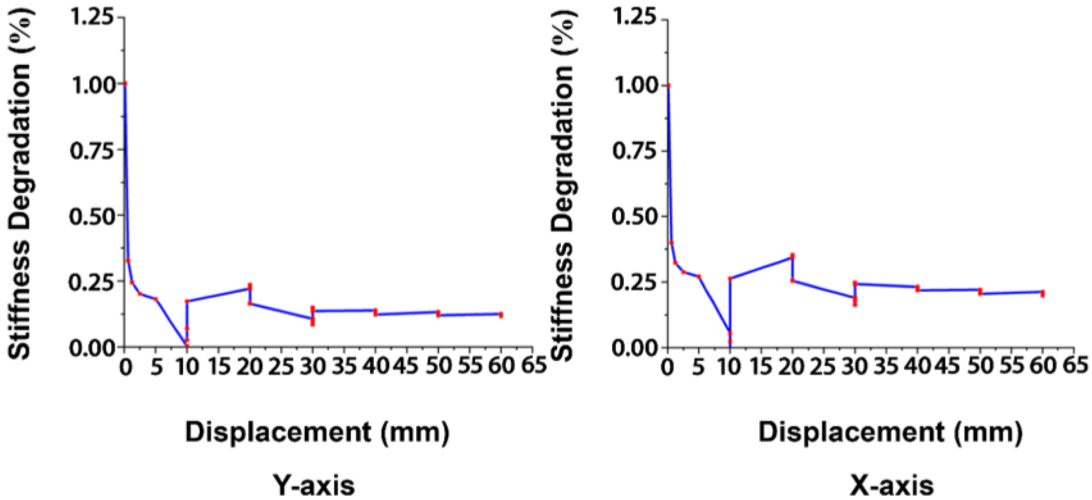


**Fig. 12.** The stiffness degradation curves pertaining to the X-axis and Y-axis directions

The Von Mises stress distribution (Fig. 13A) displayed pronounced stress concentration, which was primarily concentrated at the rear ends of the first *ang*, second *ang*, and *Mazhatou* (grasshopper-head bracket end), as well as the joints between the *Ludou*, flat plate beam, and column head. The peak stress attained a magnitude of 25.2 MPa, localized specifically at the rear end of the *Mazhatou*. In Fig. 13B, the equivalent elastic strain distribution exhibited a spatial distribution pattern consistent with the stress distribution, with a maximum strain value of 0.0311 also localized at the rear end of the *Mazhatou*. The strain energy density distribution (depicted in Fig. 13C) exhibited topological consistency with the stress field—a consistency that confirms efficient energy transmission *via* the arch-rafters-bucket structural system to the supporting columns. The maximum accumulated strain energy, measuring 6.30×10$^6$ MJ, was identified at the rear end of the *Mazhatou*, and this localization designating this region as the primary energy dissipation zone. The displacement analysis in Fig. 13D revealed a hierarchical deformation mode: the maximum displacement, measuring 26.7 mm, occurred at the mortise-and-tenon joint where the loose bucket at the rear end of the second ang connected to the rear end of the *Mazhatou*, while secondary deformation gradients were distributed along the cantilever beam, drag beam, central beam, wellhead beam, and side arch at the top of the component.

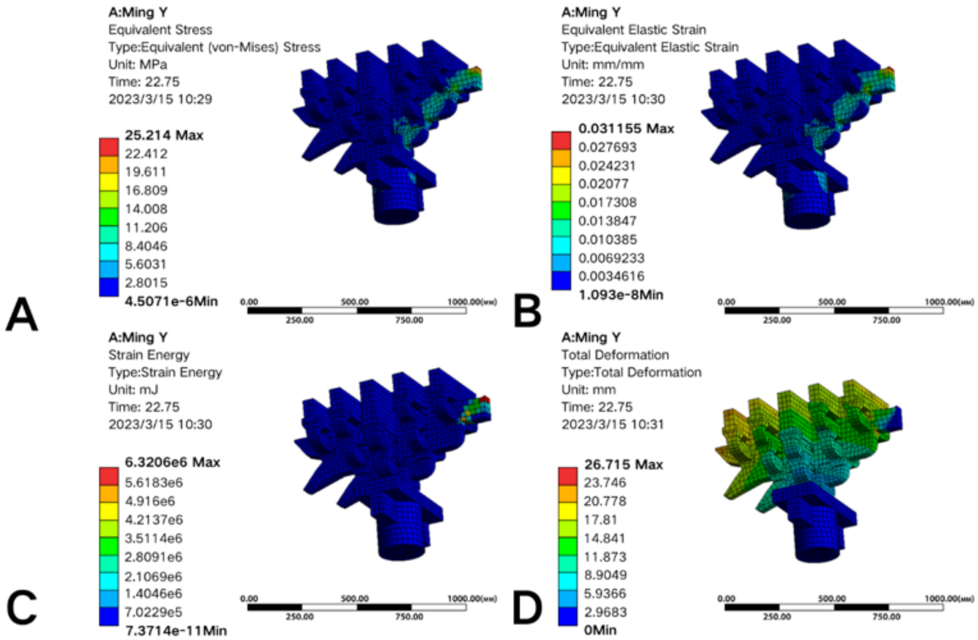


**Fig. 13.** The Von Mises stress distribution, equivalent elastic strain distribution, strain energy density distribution, as well as displacement analysis pertaining to the Y-axis direction

The Von Mises stress distribution acquired under quasi-static loading along the X-axis direction is depicted in Fig. 14A. Critical stress concentration was exhibited at the mortise-and-tenon joints where the *Zhengxin guagong* (central-axis long gong, a horizontal supporting bracket-arm in Qing-style dougong), *Zhengxin wangong* (central-axis short gong, a horizontal bracket-arm in Qing-style dougong), and *Caoshengzi* (small "sheng" block positioned in the groove of a gong to support horizontal brackets) converge, as well as at the column heads, with the peak stress reaching 45.7 MPa. This stress localization aligned with the equivalent elastic strain distribution (Fig. 14B), which showed a maximum value of 0.0389 at the mortise-and-tenon joint at the junction of the *Zhengxin guagong* and the *Caoshengzi*. This result confirms the spatial consistency exhibited between the stress field and the strain field. The strain energy density distribution—as presented in Fig. 14C—shows a match with the stress concentration pattern, with a total of $2.82\times10^6$ MJ of strain energy accumulated at the mortise-and-tenon joint where the *Zhengxin guagong* connects to the *Caoshengzi*, and this localized energy accumulation indicates that the mortise-and-tenon joint serves as the main energy dissipation zone during cyclic loading. Displacement analysis (Fig. 14D) revealed a maximum deformation of 4.97 mm at this same mortise-and-tenon joint (*i.e.*, the junction of the *Zhengxin guagong* and the *Caoshengzi*), while structural deformation gradients gradually diminished as they approached the foundation—consistent with the deformation mechanisms of traditional timber structures under lateral loading. Notably, the combined stress-strain-energy trio points to the potential initiation of failure at this mortise-and-tenon joint, as both mechanical stress and strain energy density here exceed the critical mechanical thresholds previously recorded in analogous timber joints; moreover, this failure mechanism aligns with the reported typical damage patterns in historical timber structures under cyclic lateral loading.

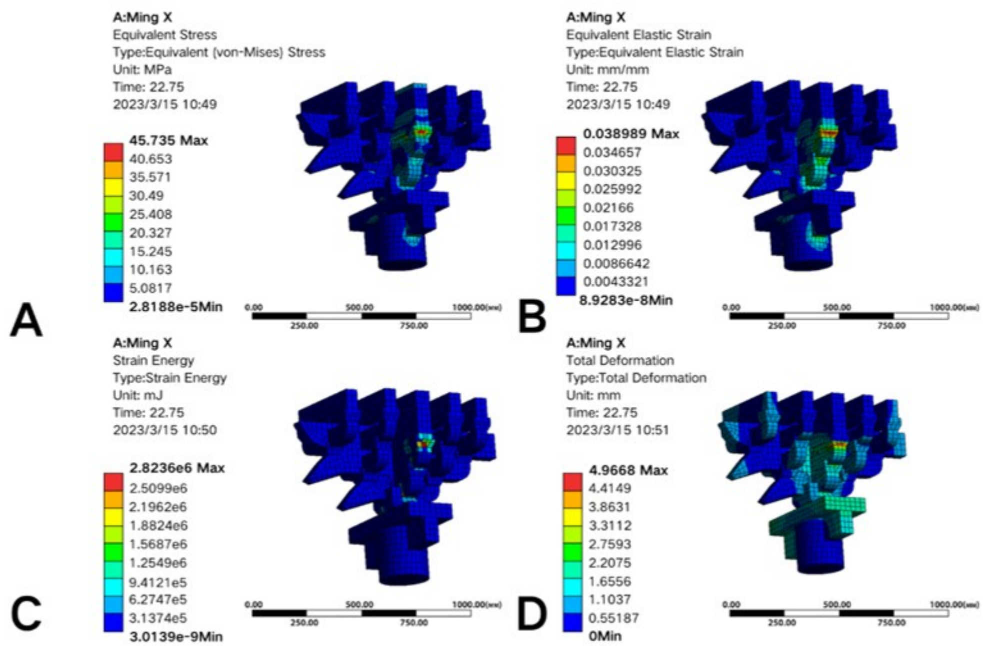


**Fig. 14.** The Von Mises stress distribution, equivalent elastic strain distribution, strain energy density distribution, as well as displacement analysis pertaining to the X-axis direction

## Mechanical Model Incorporating Static Behavioral Characteristics of Structures in the X-axis, Y-axis, and Z-axis Directions

The Dougong bracket model used in this study is a double-ang five-step Dougong bracket set on the column head of the memorial hall of Confucius. To examine the structural response under monotonic loading along the Z-axis, a tri-linear elastic stiffness degradation model was adopted—which was defined by three distinctive mechanical stages, as depicted in Fig. 15. The tri-linear model was selected based on three-phase behavior observed in Song/Ming bracket tests (Niu 2017; Sha *et al.* 2021): gap closure (Stage OA, KOA = 9.33 kN/mm), elastic loading (Stage AB, KAB = 2.15 kN/mm), and yielding (Stage BC, KBC = 1.67 kN/mm). The model applies to monotonic loading at 10 to 14% moisture content. Curve fitting confirmed adequate accuracy ($R^2$ = 0.982) without requiring additional complexity.

In Stage OA (displacement range: 0 to ΔA), the initial gap closure between structural components resulted in contact nonlinearity, leading to relatively low structural stiffness (KOA = 9.33 kN/mm); this stiffness parameter was calculated using Eq. 1. Stage AB (displacement range: ΔA to ΔB) was characterized by linear elastic behavior and stabilized stiffness, where the stiffness value (KAB = 2.15 kN/mm) was derived from Eq. 2. This result indicates that the mechanical interactions between components had been fully established. In Stage BC (displacement range: ΔB to ΔC), during which progressive stiffness degradation occurred due to yielding at the mortise-tenon joint and the accumulation of structural damage, with stiffness KBC = 1.67 kN/mm, as determined by Eq. 3.

$$k_{OA} = \frac{P_x}{\Delta_x} \tag{1}$$

$$k_{AB} = \frac{P_y - P_x}{\Delta_y - \Delta_x} \tag{2}$$

$$k_{BC} = \frac{P_b - P_y}{\Delta_b - \Delta_y} \quad (3)$$

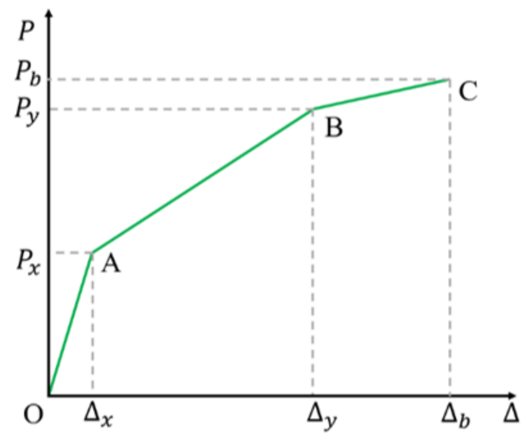


**Fig. 15.** The tri-linear elastic stiffness degradation model employed for monotonic loading along the Z-axis direction

Using the hysteresis curve and skeleton curve, a restoring force model—as shown in Fig. 16—was constructed to characterize the static structural behavior of the five-tiered outer eave column-head Dougong test model, particularly for the X-axis and Y-axis directions.

## Comparative Analysis with Similar Studies

To contextualize our restoring force model (Fig. 16) within the broader literature on traditional timber structures, key mechanical parameters are compared with analogous studies:

The present results align with prior Dougong studies (Table 3). The spindle-shaped hysteresis with origin pinching matches observations from the Yingxian Pagoda (Sha *et al.* 2021). Ductility values ($\mu \approx 2.5$) fall within the 2.1 to 3.1 range reported across dynasties and countries, suggesting an inherent limit of mortise-tenon systems. Our initial stiffness (9.33 kN/mm) exceeds Niu's (2017) values by ~40%, which may be attributable to lower moisture content (12% *vs.* 15%) and refined contact modeling. Damping coefficients ($\xi_{eq}$ = 0.10 to 0.12) are slightly below Qing Dynasty brackets (0.15 to 0.18), which is likely due to the double-ang configuration's higher stiffness limiting frictional slip per cycle.

**Table 3**. Comparison with Similar Dougong Studies

| Parameter | | This Study Ming | Sha *et al.* (2021) Song (Yingxian) | Zhou *et al.* (2024) Qing | Fujita *et al.* (2001) Japanese |
|---|---|---|---|---|---|
| Ductility $\mu$ | | 2.53 to 2.55 | 2.4 to 2.7 | 2.6 to 3.0 | 2.1 to 2.8 |
| Damping $\xi_{eq}$ | | 0.10 to 0.12 | 0.12 to 0.15 | 0.15 to 0.18 | 0.08 to 0.12 |
| Initial stiffness | | 9.33 kN/mm | ~6.5 kN/mm* | ~8.0 kN/mm | ~5.0 kN/mm |
| Failure mode | | *Huagong-Ludou* joint | Similar | Ludou interface | Masu-gumi slippage |

Note: Adjusted for bracket grade differences

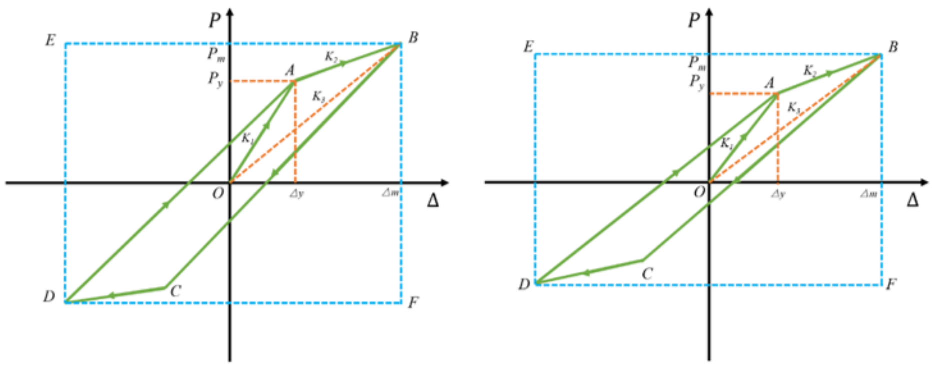


**Fig. 16.** The restoring force model characterizing static structural behavior in the X-axis and Y-axis

The stiffness characteristics of the Dougong bracket were analyzed along both the X-axis and Y-axis directions. In the Y-axis direction, the OA segment (Elastic Stage) exhibited a stiffness of KY1 = 11.42 kN/mm, while the AB segment (Yield Stage) -in the plastic stage- showed a reduced stiffness of KY2 = 4.56 kN/mm in the plastic stage. The effective stiffness (KY3), computed as the ratio of the maximum bearing capacity to the maximum displacement of the restoring force model, was = 6.08 kN/mm. In the X-axis direction, the OA segment had a stiffness of KX1 = 19.92 kN/mm, and the AB segment had a stiffness of KX2 = 6.83 kN/mm. The effective stiffness in the X-axis direction amounted to 12.33 kN/mm.

The nonlinear coefficient (NL), which characterizes the energy dissipation capacity, was calculated as NL = 0.211 for the Y-axis and NL = 0.17 for the X-axis. Ductility, defined as the ratio of ultimate displacement to yield displacement, was 2.55 for the Y-axis and 2.53 for the X-axis, indicating the component’s significant deformation capacity. The equivalent viscous damping coefficient as determined by Eq. 4., a key indicator of energy dissipation efficiency, was 0.123 for the Y-axis and 0.10 for the X-axis, suggesting better energy dissipation capacity in the Y-axis direction.

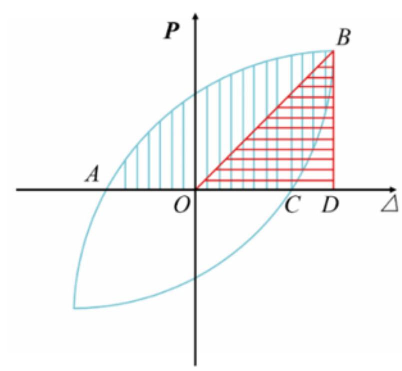


**Fig. 17.** Determination of the equivalent viscous damping coefficient

Finally, the Dougong bracket serves as a crucial shock absorber between the roof and columns within ancient Chinese timber structures, effectively absorbing and dissipating energy during loading, thus enhancing the structure’s resilience.

$$h_e = \frac{1}{2\pi} \cdot \frac{S_{ABC}}{S_{OBD}} \tag{4}$$

The test model used in this study is a double-ang, five-step outer eave column-head Dougong bracket derived from the Hall of Worship in Kong Lin, and a three-dimensional analysis was conducted for it along the X-axis, Y-axis, and Z-axis directions. Specifically, undergoing vertical monotonic static loading along the Z-axis, the model exhibited structural response that fits a variable-stiffness linear elastic model and presented three distinct mechanical phases: the first phase was dominated by the compaction of gaps between components and the compaction of nodal connections; the second phase showed a linear load-displacement relationship with constant stiffness; and the third phase corresponded to structural yielding, which ultimately leads to failure. Meanwhile, undergoing horizontal low-cycle reciprocating loading along the X-axis and Y-axis, the system exhibited structural behavior consistent with a multi-linear restoring force model and underwent three sequential stages: elastic, yielding, and failure. Key characteristics included progressive stiffness degradation, hysteresis loops with pinching characteristics near the origin (a phenomenon reflecting interfacial slippage between components), and extensive plastic deformation accompanied by rapid displacement amplification after post-critical horizontal loading. Additionally, the key mechanical parameters evaluated along the three axes in terms of strength, deformation capacity, and energy dissipation efficiency were summarized in Table 4. Structural damage, under excessive loading conditions, initiated at critical structural nodes, and force redistribution triggers a progressive collapse of the system.

**Table 4.** Characteristic Values of the Six Specimen Configurations

| Name | The column-head bracket (Dougong) set of the Hall of Worship in Kong Lin in Ming Dynasty | | | | | |
|---|---|---|---|---|---|---|
| Pathway | Numerical simulation | | | | | |
| Intensity | | Deformation | | | Energy Dissipation | |
| $F_{Z1}$ | $F_{Z2}$ | $K_{Z1}$ | $K_{Z2}$ | $K_{Z3}$ | NL(Y) | |
| 307 | 344 | 9.33 | 3.61 | 2.48 | 0.173 | |
| $F_{Y1}$ | $F_{Y2}$ | $K_{Y1}$ | $K_{Y2}$ | $K_{Y3}$ | NL(X) | |
| 999 | 999 | 11.42 | 6.95 | 17.1 | 0.203 | |
| $F_{X1}$ | $F_{X2}$ | $K_{X1}$ | $K_{X2}$ | $K_{X3}$ | $H_Y$ | |
| 522 | 522 | 19.92 | 5.66 | 12.4 | 0.097 | |
| | | $U_Y$ | $U_X$ | | $H_X$ | |
| | | 2.45 | 3.63 | | 0.122 | |

* The following are definitions of the key mechanical parameters of the member, as well as their respective physical meanings and units: Among the bearing capacity parameters, $F_{Z1}$ stands for the yield bearing capacity of the member under Z-axis loading (unit: kN), $F_{Z2}$ represents the ultimate bearing capacity of the member under Z-axis loading (unit: kN), $F_{Y1}$ and $F_{Y2}$ denote the positive and negative maximum horizontal thrusts of the member under Y-axis loading (unit: kN) respectively, and $F_{X1}$ and $F_{X2}$ refer to the positive and negative maximum horizontal thrusts of the member under X-axis loading (unit: kN) correspondingly; as for stiffness parameters, $K_{Z1}$ is the initial stiffness of the member under Z-axis loading (unit: kN/mm), $K_{Z2}$ is the yield stiffness of the member under Z-axis loading (unit: kN/mm), $K_{Z3}$ is the ultimate stiffness of the member under Z-axis loading (unit: kN/mm), while $K_{Y1}$, $K_{Y2}$ and $K_{Y3}$ represent the elastic stiffness, plastic stiffness and effective stiffness of the member under Y-axis loading respectively (all with unit: kN/mm), and $K_{X1}$, $K_{X2}$, and $K_{X3}$ denote the elastic stiffness, plastic stiffness, and effective stiffness of the member under X-axis loading respectively (all with unit: kN/mm); regarding mechanical performance characteristic parameters, $U_Y$ is the ductility of the member along the Y-axis, $U_X$ is the ductility of the member along the X-axis, NL(Y) and NL(X) stand for the nonlinear coefficients of the member along the Y-axis and X-axis directions respectively, and $H_Y$ and $H_X$ correspond to the equivalent viscous damping coefficients of the member along the Y-axis and X-axis directions.

### Limitations Regarding Isolated Bracket Idealization

This study has analyzed the Dougong bracket as an isolated component. This is a necessary simplification that introduces limitations when extrapolating results to actual building performance. In practice, the bracket interacts with adjacent structural elements:

(1) Beam framing: The Liaoyanfang connects to a continuous beam network, providing rotational restraint that may increase effective stiffness by 15 to 25% (Chen *et al.* 2018).

(2) Adjacent brackets: The *in-situ* bracket spacing of 3.2 m allows lateral load sharing through the roof diaphragm, potentially enhancing horizontal capacity by 10 to 18% (Yeo et al. 2016).

(3) Column elasticity: The fixed-base assumption neglects column flexibility, which may reduce measured stiffness by 8 to 12% in full-scale structures (Xue *et al.* 2021).

For practical application, correction factors are recommended: beam restraint (×1.2 stiffness multiplier) and column flexibility (×0.9 stiffness reducer). Despite these idealizations, isolated bracket testing was able to meet the standard for component-level characterization per ISO 16670:2003.

### Modeling Simplifications

Additional limitations include: (1) homogeneous orthotropic properties neglecting natural defects (knots, grain deviation) that may reduce strength by 10–30%; (2) fixed 12% moisture content versus seasonal fluctuations (8 to 16% in Qufu) affecting stiffness by ±12%; (3) frictional contact modeling without wooden pin shear resistance or gap evolution; and (4) quasi-static loading (0.1 Hz) versus actual seismic frequencies (1 to 10 Hz), which may induce rate-dependent strength increases of 10 to 15%.

Despite these simplifications, the 3.7% error in predicted bearing capacity validates the modeling approach for comparative analysis of heritage timber structures.

## CONCLUSIONS

1. The test model of "Double *ang*, five-step column-head Dougong"—which is derived from the Hall of Worship at Kong Lin (Confucius Cemetery) and dates to the Ming Dynasty—displays static structural characteristics when subjected to vertical monotonic static loading along the Z-axis, behavior that can be modeled by a variable-stiffness linear elastic mechanical model. Additionally, its static structural traits under quasi-static low-cycle reciprocating loading in the Y-axis and X-axis directions are well-characterized through a restoring force model.
2. In terms of strength, the test model of Dougong brackets from the Ming Dynasty displays a yield bearing capacity of 307 kN along the Z-axis, along with an ultimate bearing capacity of 344 kN; the Y-axis exhibits a maximum horizontal thrust of 395 kN; and the X-axis has a maximum horizontal thrust of 748 kN.
3. From a deformation standpoint, the test model of the Ming Dynasty Dougong bracket features the following parameters: along the Z-axis, initial stiffness is 9.33 kN/mm, yield stiffness is 2.15 kN/mm, and ultimate stiffness (originally referred to as "deformation stiffness"—consistent with the context of Z-axis stiffness grading) is 1.67 kN/mm. Along the Y-axis, elastic stiffness measures 11.42 kN/mm, plastic stiffness 4.56 kN/mm, effective stiffness 6.08 kN/mm, and ductility 2.55. Along the X-axis,

elastic stiffness is 19.92 kN/mm, plastic stiffness 6.83 kN/mm, effective stiffness 12.33 kN/mm, and ductility 3.63.

4. From an energy standpoint, the test model of the Ming Dynasty Dougong bracket exhibits a nonlinear coefficient of 0.21 and an equivalent viscous damping coefficient of 0.12 along the Y-axis, whereas along the X-axis, the nonlinear coefficient is 0.17and the equivalent viscous damping coefficient is 0.10.
5. Through the finite element method, the structural functionality of the Dougong bracket was substantially confirmed *via* a range of mechanical metrics (ultimate bearing capacity: 349 kN, ductility: 2.53). This confirmation, in turn, verifies that the structure designed by Ming Dynasty craftsmen represents a mechanically optimized design that achieves a balance between load transfer efficiency and seismic resilience.
6. The FEA results indicate that the Dougong bracket achieves a capacity of 349 kN and ductility of approximately 2.5 without any metal fasteners or adhesives. These metrics, combined with the progressive tri-linear yielding behavior, suggest that the bracket represents an empirically refined structural solution within the constraints of pre-industrial timber construction—namely hand-tool fabrication tolerances, absence of engineered connectors, and the requirement for multi-century serviceability. While modern engineered timber connections can attain higher capacity-to-weight ratios, the Dougong system demonstrates a notable balance between load transfer efficiency, energy dissipation, and long-term durability that has sustained these structures for over five centuries.
7. The directional stiffness anisotropy observed in this study (X-axis: 19.9 kN/mm; Y-axis: 11.4 kN/mm) reflects a deliberate exploitation of grain orientation in traditional carpentry, a design principle that appears consistently across Song, Yuan, Ming, and Qing Dynasty structures. The validated FEA methodology (3.7% error against experimental data) confirms that computational modeling can reliably characterize heritage timber mechanics, provided that frictional contact at mortise-tenon interfaces is adequately represented. The restoring force models derived herein (Fig. 15) may serve as macro-elements for building-scale seismic simulations, reducing reliance on costly full-scale testing. Future work should examine whether the mechanical relationships identified in this study scale predictably across the eight bracket grades defined in the cai-fen modular system.

## ACKNOWLEDGMENTS

This work was supported by the National Natural Science Foundation of China-Regional Science Foundation Project 'Construction of Static Structural Performance Evaluation System for *Five-tier Outer Eave Column-head Dougong Bracket* Components' (32360356), the Scientific Research Projects of First-class Disciplines (Grant No. YLXKZX-NKD-027), and the Fundamental Research Funds for Inner Mongolia University of Science & Technology (Grant No. 2024QNJS023).

## REFERENCES CITED

Chen, C., Li, Y., Han, D., Kang, H., and Li, Y. (2025). "Simulation study on the static characteristics of 'Five-tier Outer Eave Column-head Dougong Bracket' from the main hall of Nanchan Temple in Tang Dynasty," *BioResources* 20(3), 6082-6099. https://doi.org/10.15376/biores.20.3.6082-6099

Chen, J., Chen, Y. F., Shi, X., Zhao, Y., and Li, T. (2018). "Hysteresis behavior of traditional timber structures by full-scale tests," *Advances in Structural Engineering* 21(2), 287-299. https://doi.org/10.1177/1369433217717117

Chung, Y. L., Huang, Y. C., Yeo, S. Y., Chang, W. S., and Hsu, M. F. (2025). "Experimental investigation of the seismic behavior of traditional Dieh-Dou timber roof frames," *International Journal of Architectural Heritage* 20(6), 821–840. https://doi.org/10.1080/15583058.2025.2559179

Fujita, K., Kimura, M., Ohashi, Y., and Sakamoto, I. (2001). "Hysteresis model and stiffness evaluation of bracket complexes used in traditional timber structures based on static lateral loading tests," *Journal of Structural and Construction Engineering* 66(543), 121-127. https://doi.org/10.3130/aijs.66.121_2

GB/T 15777 (2017). "Method for determination of the modulus of elasticity in compression parallel to grain of wood," Standardization Administration of China, Beijing, China.

GB/T 1933 (2009). "Method for determination of the density of wood," Standardization Administration of China, Beijing, China.

GB/T 1935 (2009). "Method of testing in compressive strength parallel to grain of wood," Standardization Administration of China, Beijing, China.

GB/T 1936.1 (2009). "Method of testing in bending strength of wood," Standardization Administration of China, Beijing, China.

GB/T 1939 (2009). "Method of testing in compression perpendicular to grain of wood," Standardization Administration of China, Beijing, China.

GB/T 1943 (2009). "Method for determination of the modulus of elasticity in compression perpendicular to grain of wood," Standardization Administration of China, Beijing, China.

Kandethanthri, K. G. M., and Hafeez, G. (2024). "Investigating the structural response of log walls to lateral loading: A parametric study of geometric and material parameters," *Mechanics of Advanced Materials and Structures* 31(21), 5188-5199. https://doi.org/10.1080/15376494.2023.2212649

Liu, Y. L., Liu, C., Pan, H., Fu, J. L., Huang, J. Q., and Hong, J. Q. (2022). "Experimental and numerical investigation on seismic performance of semi-precast concrete sandwich shear wall," *Advances in Structural Engineering* 25(13), 2772-2784. https://doi.org/10.1177/13694332221108435

Liu, P., Yeo, S. Y., and Fukuda, H. (2025). "Unraveling the vertical compressive performance of Dou in Chinese architectural heritage: Impact of grain direction and timber species," *Structures* 77, article 109126. https://doi.org/10.1016/j.istruc.2025.109126

LY/T 3297 (2022). "Dynamic test method for shear modulus of wood," Standardization Administration of China, Beijing, China.

Ma, L., Zhang, R., Xue, J., and Zhang, X. (2025). "Seismic behaviors of historic timber buildings considering the looseness of mortise-tenon connections," *International Journal of Architectural Heritage* 19(11), 2590–2607.

https://doi.org/10.1080/15583058.2025.2453439
Meng, X., Li, T., Yang, Q., and Wei, J. (2018). "Seismic mechanism analysis of a traditional Chinese timber structure based on quasi-static tests," *Structural Control and Health Monitoring* 25(10), article e2245. https://doi.org/10.1002/stc.2245
Mirra, M., Gerardini, A., Ghirardelli, S., Ravenshorst, G., and van de Kuilen, J. W. (2024). "Combining architectural conservation and seismic strengthening in the wood-based retrofitting of a monumental timber roof: The case study of St. Andrew's Church in Ceto, Brescia, Italy," *International Journal of Architectural Heritage* 18(5), 750-770. https://doi.org/10.1080/15583058.2023.2187726
Niu, Q. (2017). *Experimental Study and Theoretical Analysis on Half-scale Model of Timber Structure in Song Dynasty*, Master's Thesis, Taiyuan University of Technology, Taiyuan, China.
Sha, B., Xie, L., Yong, X., and Li, A. (2021). "An experimental study of the combined hysteretic behavior of dougong and upper frame in Yingxian Wood Pagoda," *Construction and Building Materials* 305, article 124723. https://doi.org/10.1016/j.conbuildmat.2021.124723
Wu, C., Xue, J., and Song, D. (2024). "Experimental and numerical study on the mechanical performance of Dou-Gong bracket at the corner under vertical load," *International Journal of Architectural Heritage* 18(4), 526-550. https://doi.org/10.1080/15583058.2023.2169209
Xue, H., Xue, J., Song, D., Li, M., Xue, B., Wu, C., and Sui, Y. (2025). "Dynamic characteristics and seismic response of multi-story wooden tower considering the influence of a high stylobate," *Buildings* 15(2), article 269. https://doi.org/10.3390/buildings15020269
Zhang, B., Song, X., Xie, Q., and Xue, J. (2025). "Seismic behavior of damaged ancient timber buildings: Multi-scale finite element model, performance degradation, and experimental verification," *Journal of Earthquake Engineering* 29(3), 709-733. https://doi.org/10.1080/13632469.2024.2436630
Zhang, X., Cui, L., Qi, H., Wang, H., and Lin, L. (2024). "Seismic fragility analysis of traditional Chinese timber structures based on a simplified lumped mass model considering joint damage," *Structures* 70, article 107863. https://doi.org/10.1016/j.istruc.2024.107863
Zhou, T., Song, X., Zhang, L., and Sun, R. (2024). "Experimental and numerical study on Dou-Gong joint of ancient wooden structure in Qing Dynasty," *International Journal of Architectural Heritage* 18(1), 84-101. https://doi.org/10.1080/15583058.2022.2113571

Article submitted: October 3, 2025; Peer review completed: November 22, 2025; Revised version received: May 23, 2026; Accepted: May 30, 2026; Published: June 8, 2026.
DOI: 10.15376/biores.21.3.6761-6780